

Single and two-cells shape analysis from energy functionals for three-dimensional vertex models

Ahmad K. Khan¹, Cécilia Olivesi², Jose J. Muñoz^{*1,2,3,4}

February 9, 2023

¹ Universitat Politècnica de Catalunya, 08034 Barcelona, Spain.

² Laboratori de Càlcul Numèric (LaCàN), Universitat Politècnica de Catalunya, 08034 Barcelona, Spain.

³ Centre Internacional de Mètodes Numèrics en Enginyeria (CIMNE), 08034 Barcelona, Spain.

⁴ Institut de Matemàtiques de la UPC -BarcelonaTech (IMTech), 08028 Barcelona, Spain.

Abstract

Vertex models have been extensively used for simulating the evolution of multicellular systems, and have given rise to important global properties concerning their macroscopic rheology or jamming transitions. These models are based on the definition of an energy functional, which fully determines the cellular response and conclusions. While two-dimensional vertex models have been widely employed, three-dimensional models are far more scarce, mainly due to the large amount of configurations that they may adopt and the complex geometrical transitions they undergo. We here investigate the shape of single and two-cells configurations as a function of the energy terms, and we study the dependence of the final shape on the model parameters: namely the exponent of the term penalising cell-cell adhesion and surface contractility. In single cell analysis, we deduce analytically the radius and limit values of the contractility for linear and quadratic surface energy terms, in 2D and 3D. In two-cells systems, we deduce the evolution of the aspect ratio. While in functionals with linear surface terms yield the same aspect ratio in 2D and 3D, the configurations when using quadratic surface terms are distinct. We relate our results with

well-known solutions from capillarity theory, and verify our analytical findings with a three-dimensional vertex model.

*Jose J. Muñoz. j.munoz@upc.edu

keywords: vertex models, cells, droplets, contractility, adhesion.

1 Introduction

Many fundamental embryonic developmental processes are driven by inter- and intra-cellular mechanics, which determine epithelial and tissue shape changes [1]. The interplay between the elasticity of the cell, cortical contractility and adhesion at the junctions influence macroscopic shape evolution [2]. However, while cellular deformations and tissue reorganisation can be directly measured, forces can be only computed in indirect manner, by either using specific sensors [3, 4, 5] or resorting to specific computational models and numerical techniques, such as Cellular Potts [6], Finite Element [7, 8, 9], vertex models [10], or particle methods [11, 12, 13], to cite a few. These models require though the knowledge of material properties and chemomechanical interaction, which in many cases can be only estimated.

At the cellular scale, due to the explicit representation of cell boundaries, vertex models have been exploited to simulate tissue rheology and evolution from cellular mechanics [10]. Initially, the vertex models were developed to understand the groups of joint bubbles in foams [14, 15]. Vertex models discretise epithelial cells by a set of vertices [10, 16] and impose static or dynamic equilibrium jointly by volumetric constraints. As such, they are equally valid to describe cell packings or capillarity problems composed of bubble-like bodies. Although our aim is to analyse cellular geometries, our result can be also applied to non-biological problems driven by surface area minimisation and volumetric constraints.

Two-dimensional vertex models have been widely exploited to describe fluidity of tissues [17], topological transitions [18, 19, 20, 21] or jamming [22]. Three-dimensional extensions have been developed for epithelial rheology [23, 24], folding [25], blastocytes analysis [26], wound healing [27], cyst formation [28], or cell division [29], to cite a few.

Vertex models require the definition of a functional that depends on the vertex coordinates $\mathbf{y} = \{\mathbf{y}_1, \dots, \mathbf{y}_{N_{vert}}\}$, which is minimised with respect to each vertex position \mathbf{y}_I , $I = 1, \dots, N_{vert}$. In fact, the form of this functional determines the forces at equilibrium, and the global predictions that we can derive from the model. The general form of the energy functional depends explicitly on geometrical measures of

the cell, and may be expressed in two dimensions (2D) as

$$W_{2D}(\mathbf{y}) = \lambda \sum_i (A_i - A_0)^{n_V} + \Gamma \sum_i P_i^{n_P} + \sum_{m,n} \Lambda_{mn} l_{mn}^{n_L} \quad (1)$$

where A_i and P_i are respectively the area and perimeter of the cell i , A_0 a reference preferential area, λ and Γ the area and perimeter modulus, l_{mn} is the length between vertices m and n and Λ_{mn} the tension of segment $\mathbf{y}_m - \mathbf{y}_n$. The equivalent form of the functional in three dimensions (3D) reads,

$$W_{3D}(\mathbf{y}) = \sigma \sum_e l_e^{n_L} + \lambda_e \sum_e A_e^{n_{A_e}} + \lambda_c \sum_c A_c^{n_{A_c}} + \lambda_v \sum_i (V_i - V_0)^{n_V} \quad (2)$$

with V_0 a preferential reference volume. Parameters λ_c and λ_e represent penalisation of different surface areas (cell-cell vs cell-environment, lateral vs basal, etc). Depending on the biological problem, some authors have considered additional terms for bending [30], or hybrid energy definitions with 3D vertex coordinates but with cells located on a two dimensional manifold, and with additional normal pressure forces and constraints [31, 25].

The functionals $W_{2D}(\mathbf{y})$ and $W_{3D}(\mathbf{y})$ additionally depend on the exponents n_V , n_P , n_L , n_{A_r} and n_{A_c} . In the literature, there is a general agreement in using quadratic terms for area and volume penalisation in 2D and 3D, respectively, that is, in using $n_V = 2$, which is tantamount to reduce volume variations. However, the exponents of other terms may vary depending on the authors and applications. Tables 1 and 2 show some of the values of the exponents for surface energy term (perimeter in 2D). The use of quadratic terms, i.e. $n_P = 2$, may be interpreted as an elastic response, where the resulting forces $\mathbf{g}_I = \partial_{\mathbf{y}_I} W$ are proportional to the area (or perimeter in 2D). Instead, in linear functionals with $n_A = n_P = 1$, the forces do not vary as area or perimeter increases, and are thus more pertinent for fluid-like behaviour, where the constants $\Gamma, \lambda, \lambda_c, \lambda_e$ represent surface tensions.

The objective of the present work is to analyse the effects on the resulting shape when using linear or quadratic functionals, for simple cell configurations, and study their differences in 2D and 3D models. We will derive in Section 2 some analytical results for single and two-cells configurations, and in the latter case, focus on the aspect ratio or relative area of the cell-cell surface. We will assume axial symmetry, and thus our system is fully defined by the radius r of a single cell, or the radius and parameter h , corresponding to half distance of the maximum overlapping, as indicated in Figure 1. In Section 3 we will verify our theoretical results with a numerical 3D vertex model.

Reference	Line (n_L)	Perimeter (n_P)	Area (n_V)
Duclut et al. [32], Barton et al. [33], Osterfield et al. [34] Fletcher et al. [35], Farhadifar et al. [19]	1	2	2
Bi et al. [22], [36]	-	1,2	2
Spencer et al. [37], Cavanaugh et al. [38]	1	-	2
Mossaffa et al. [39], [40], [41],	2	-	2

Table 1: Order of exponent in different terms in 2D vertex models. See equation (1).

Reference	Line (n_L)	Surface Area e (n_{A_e})	Surface Area c (n_{A_c})	Volume (n_V)
Honda et al [42, 26]	-	1	1	2
Okuda et al. [43]	2	1	2	2
Fang et al [30]	1	-	2	2
Misra et al [44]	1	1	1	2
Ioannou et al. [27]	2	2	2	2

Table 2: Order of exponent in different terms in 3D vertex models. See equation (2).

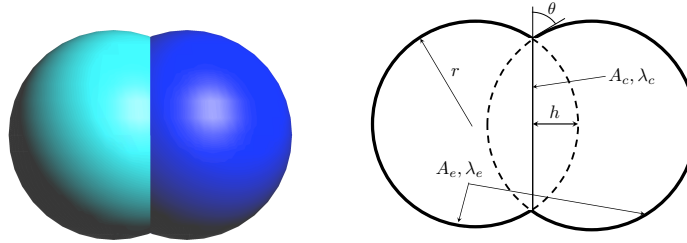


Figure 1: Illustration of two-cells systems (left) and geometrical parameters (r, h) (right).

2 Analytical results

In the following derivations we initially assume a three-dimensional energy functional, which we will adapt for comparing our results with two-dimensional configurations. A quadratic term for the volume penalisation is assumed ($n_V = 2$), while we consider two possible values of the surface exponent, $n_A = 1$ (linear functional) and $n_A = 2$ (quadratic functional). More precisely, the following general expression of the energy functional is studied,

$$W(r, h) = \frac{1}{2} \sum_i^N \left(\frac{V_i - V_0}{V_0} \right)^2 + \frac{\lambda_c}{n_A} \left(\frac{A_c}{A_0} \right)^{n_A} + \frac{\lambda_e}{n_A} \sum_i^{N_e} \left(\frac{A_{e_i}}{A_0} \right)^{n_A} \quad (3)$$

with $V_i(r, h)$ the volume of cell i , $A_c(r, h)$ the interface area between the two cells, and $A_{e_i}(r, h)$ the external area of cell i . We restrain our analysis to one cell and two cells, i.e. $N = \{1, 2\}$. For $N = 1$, we set $A_c = 0$ and assume radial symmetry, while for $N = 2$ we consider cylindrical symmetry with respect to the axis joining the two cells centres. The values V_0 and A_0 are the reference volume and areas, respectively, and $r_0 = \sqrt[3]{\frac{3}{4\pi} V_0} = \sqrt{\frac{A_0}{4\pi}}$ the reference radius. Note that in our analysis, we use the same exponent n_A for all surface area terms.

2.1 Single cell analysis

Linear functional. Due to the absence of interface surface, we ignore the second term (3), and deduce the radius of equilibrium as the value of r that minimises the following functional,

$$W_L^1(r) = \frac{1}{2} \left(\frac{V(r) - V_0}{V_0} \right)^2 + \frac{\lambda_e}{2} \frac{A(r)}{A_0}, \quad (4)$$

with $V(r) = 4\pi r^3/3$ and $A(r) = 4\pi r^2$. The optimality condition $dW_L^1(r)/dr = 0$ may be expressed as,

$$r \left(V_0 - \frac{4}{3} \pi r^3 \right) - \frac{V_0^2}{A_0} \lambda_e = 0. \quad (5)$$

Real roots of the function above in the interval of interest $r \in (0, r_0)$ only exist if the surface tension λ_e is lower than a critical value,

$$\lambda_{crit} = \frac{3A_0}{4V_0} \sqrt[3]{\frac{3V_0}{16\pi}}. \quad (6)$$

Above this value, the functional W_L^1 is a monotonically increasing function for $r \geq 0$, and thus the minimiser corresponds to the degenerated configuration $r = 0$. For $\lambda_e < \lambda_{crit}$, there are two positive real

roots. We consider the largest one, which converges towards r_0 as λ_e decreases towards 0.

Quadratic functional. The energy functional for $n_A = 2$ reads

$$W_Q^1(r) = \frac{1}{2} \left(\frac{V(r) - V_0}{V_0} \right)^2 + \frac{\lambda_e}{2} \left(\frac{A(r)}{A_0} \right)^2, \quad (7)$$

which implies the following optimality condition,

$$r \left(r^2 + 6\lambda_e \frac{V_0^2}{A_0^2} \right) - r_0^3 = 0. \quad (8)$$

In view of the equation, and as expected, for $\lambda_e = 0$, the optimal radius is $r = r_0$, while for $\lambda_e > 0$, there is always at least one real positive root. The roots of (5) and (8) as a function of λ_e are shown in Figure 2. It can be checked that the optimal radius is reduced in a more pronounced manner with respect to changes in λ_e in the quadratic case, while in the linear case the cell collapses for $\lambda_e \geq \lambda_{crit}$.

Similar analysis in two dimensions yields an equivalent critical value of λ_e for linear functionals ($n_A = 1$), given by $\lambda_{crit}^{2D}(n_A = 1) = \frac{4P_0}{3A_0} \sqrt{\frac{A_0}{3\pi}}$, with A_0 and P_0 reference area and perimeter. In contrast to the three-dimensional case though, a quadratic functional ($n_A = 2$) in 2D exhibits also a critical value $\lambda_{crit}^{2D}(n_A = 2) = \frac{P_0^2}{2\pi A_0}$. Beyond this value, no solution exists other than the degenerated value $r = 0$. These results show that reduced 2D models have strong qualitative differences, and care must be taken when calibrating surface tension.

Figure 2 shows the value of r that minimises the energy functional for two and three dimensions. The critical values of λ are indicated with thick dots. It can be observed that the sole case that admits unbounded values of λ_e is the quadratic functional in 3D.

2.2 Two-cells system analysis

After assuming axi-symmetric configuration, where the volume and areas are defined as a function of spherical radius r and overlapping distance h (half of the maximum overlapping length, see Figure 1), the volume, the external area and the common interface area of the two cells can be expressed as,

$$\begin{aligned} V(r, h) &= \frac{4}{3}\pi r^3 - \pi h^2 r + \frac{1}{3}\pi h^3, \\ A_e(r, h) &= 2r\pi(2r - h), \\ A_c(r, h) &= \pi h(2r - h). \end{aligned} \quad (9)$$

In order to analyse the resulting shape, we will use the *shape factor* h/r . Due to the symmetry assumptions, the energy due to the

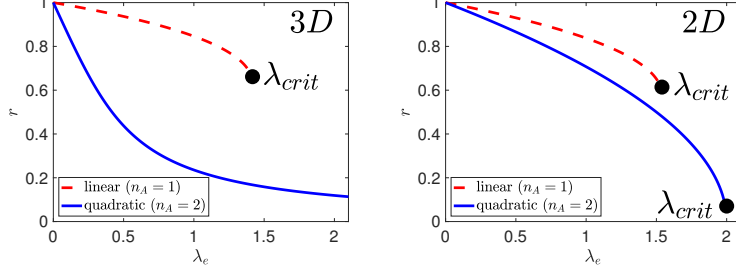


Figure 2: Evolution of r as a function of λ_e for single cell, linear and quadratic functionals. Left: results for 3D ($A_0 = 4\pi$, $V_0 = \frac{4}{3}\pi$, which implies $\lambda_{crit} = 1.417$, according to Eqn. (6)). Right: results for 2D ($A_0 = \pi$, $P_0 = 2\pi$, which yields $\lambda_{crit}(n_A = 1) = 1.54$ and $\lambda_{crit}(n_A = 2) = 2$).

contributions of the two cells reads,

$$W^2(r, h) = \left(\frac{V(r, h) - V_0}{V_0} \right)^2 + \frac{\lambda_c}{n_A} \left(\frac{A_c(r, h)}{A_0} \right)^{n_A} + \frac{\lambda_e}{n_A} \left(\frac{A_e(r, h)}{A_0} \right)^{n_A} \quad (10)$$

In the next paragraphs we deduce the values of (h, r) that minimise this functional in the linear ($n_A = 1$) and quadratic cases ($n_A = 2$).

Linear functional The optimal values of r and h are those that minimise the gradient, i.e. $\nabla W(r^*, h^*) = \mathbf{0}$, with $\nabla(\bullet) = (\partial_r, \partial_h)(\bullet)$. These conditions can be written as,

$$\frac{1}{V_0} \left(\frac{V}{V_0} - 1 \right) \nabla V + \frac{\lambda_c}{A_0} \nabla A_c + \frac{\lambda_e}{A_0} \nabla A_e = 0 \quad (11)$$

This is a system of two non-linear equations. By isolating the term $(V/V_0 - 1)/V_0$ from one of them, we obtain,

$$\frac{\lambda_c}{\lambda_e} = \left(\partial_r A_c - \partial_h A_c \frac{\partial_r V}{\partial_h V} \right)^{-1} \left(\partial_h A_e \frac{\partial_r V}{\partial_h V} - \partial_r A_e \right) \quad (12)$$

which after using the expressions in (9) yields,

$$\frac{\lambda_c}{\lambda_e} = 1 - \frac{h}{r} \quad (13)$$

Two important conclusions can be derived: the shape factor h/r is independent of A_0 and V_0 , and this factor solely depends on the ratio of the penalty terms λ_e/λ_c , but not on their actual values. Also note that we are interested in optimal values (r^*, h^*) different from the trivial solution $(r^*, h^*) = (0, 0)$, which is also a solution of (11).

Quadratic functional After setting $n_A = 2$ in (10), the equilibrium equations $\nabla W = \mathbf{0}$ now become,

$$\frac{1}{V_0} \left(\frac{V}{V_0} - 1 \right) \nabla V + \frac{\lambda_c A_c}{A_0^2} \nabla A_c + \frac{\lambda_e A_e}{A_0^2} \nabla A_e = \mathbf{0}. \quad (14)$$

By replacing the factor $(V/V_0 - 1)/V_0$ from one of the equations we find that

$$\frac{\lambda_c}{\lambda_e} = \frac{2}{h/r} - 2. \quad (15)$$

It is interesting to compare the results in (13)-(15) with those obtained in two dimensions. This simplified model is reasonable for elongated columnar cells, but is commonly used in 2D vertex models, which motivates our analysis. By replacing the volume by the area (A) and the surface area by the perimeter (P) in equations 11 and 14, and using the following expressions of these measures,

$$\begin{aligned} A &= \sqrt{h(2r-h)}(r-h) + r^2(\pi - \theta) \\ P_c &= 2\sqrt{h(2r-h)} \\ P_e &= 2r(\pi - \theta) \end{aligned} \quad (16)$$

with $\theta = \arccos((r-h)/r)$ is half of the opening angle of the contact interface, (see Figure 1), the following relations between the ratio λ_c/λ_e and the shape factor are obtained,

$$2D : \text{Linear } (n_A = 1) : \quad \frac{\lambda_c}{\lambda_e} = 1 - \frac{h}{r} \quad (17)$$

$$2D : \text{Quadratic } (n_A = 2) : \quad \frac{\lambda_c}{\lambda_e} = \frac{\pi - \theta}{\sqrt{\frac{h}{r} \left(2 - \frac{h}{r} \right)}} \left(1 - \frac{h}{r} \right) \quad (18)$$

While the linear functional gives the same relation between λ_c/λ_e and the shape factor h/r for two and three dimensions, the quadratic functional differs, despite giving similar trends. Figure 3 shows the evolution of the shape factor h/r as a function of the ratio (λ_e, λ_c) for all the studied cases. We remark that: while in the quadratic case, the cells split ($h/r = 0$) only when $\lambda_e = 0$, in the linear case this happens whenever $\lambda_c \geq \lambda_e$. Moreover, the shape factor h/r is proportional to λ_c in the linear case, while in the quadratic case is non-linear, and converges towards $h/r = 0$ as λ_c/λ_e increases. In both cases, the single spherical shape ($h = r$) is recovered when $\lambda_c = 0$ and $\lambda_e > 0$. Figure 4a shows the value of h/r on the parameter plane (λ_c, λ_e) .

Contact angles The contact angle of a contractile adhesive sphere is a usual measure for describing the mechanics of cells in contact with a substrate [45, 46]. We here compare our findings with these results,

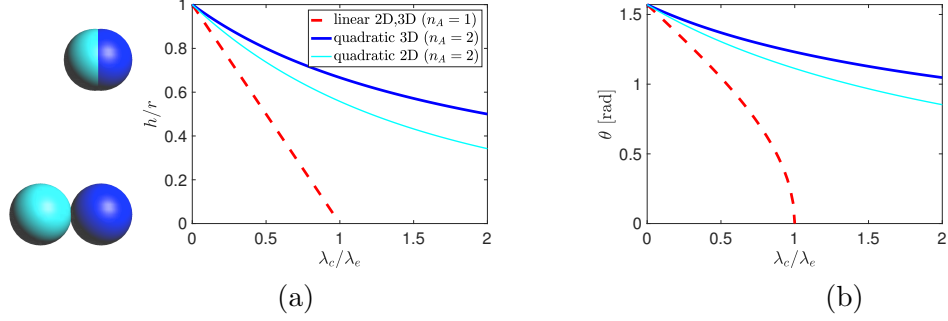


Figure 3: Evolution of shape factor h/r (a) and contact angle θ (b) in two cell-system as a function of ratio λ_c/λ_e for the linear and quadratic functional in 2D and 3D.

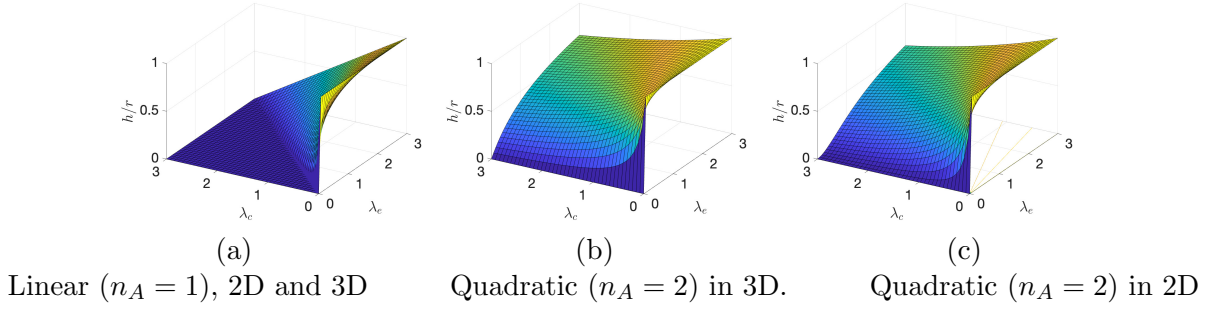


Figure 4: Shape factor h/r on the phase parameter (λ_e, λ_c) for different cases.

which assume a linear energy dependence, and are thus only valid for a linear functional ($n_A = 1$).

The relation of contact angle θ indicated in Figure 1 with the shape factor h/r can be deduced using simple geometrical arguments,

$$\cos \theta = \frac{r - h}{r} = 1 - \frac{h}{r} \quad (19)$$

Furthermore, from capillarity theory, and in the absence of an adhesive solid substrate, we have from tension equilibrium that [46],

$$\lambda_c = \lambda_e \cos \theta, \quad (20)$$

which together with (19) yields our results in (13) and (17) for a linear functional, where the penalty parameters play the role of surface tension. If a quadratic functional is used instead, relations in (17) and

(19) allow us to write

$$\frac{\lambda_c}{\lambda_e} = \frac{2}{1 - \cos \theta} - 2$$

Therefore, when using a quadratic term in the energy functional, the factor λ_c/λ_e also fully determines the shape factor and the contact angle θ , but in a different manner to the results in capillary theory. Figure 4b shows the trend of the angle as a function of the factor λ_c/λ_e .

3 Computational model

3.1 Vertex Model

We aim at verifying the previous results with a vertex model, where cell surface triangularised with a set of vertices \mathbf{y}_i . A discrete version of the energy functional can be then built from the set of vertices $\mathbf{y} = \{\mathbf{y}_1, \dots, \mathbf{y}_N\}$ and by defining the volume discrete measures of cell area and volume:

$$\begin{aligned} A^h(\mathbf{y}) &= \frac{1}{2} \sum_{e \in C} \|(\mathbf{y}_2^e - \mathbf{y}_1^e) \times (\mathbf{y}_3^e - \mathbf{y}_1^e)\| = \frac{1}{2} \sum_{e \in C} \|\mathbf{y}_1^e \times \mathbf{y}_2^e + \mathbf{y}_2^e \times \mathbf{y}_3^e + \mathbf{y}_3^e \times \mathbf{y}_1^e\| \\ V^h(\mathbf{y}) &= \frac{1}{6} \sum_{e \in C} \det(\mathbf{y}_1^e - \mathbf{y}_c^e, \mathbf{y}_2^e - \mathbf{y}_c^e, \mathbf{y}_3^e - \mathbf{y}_c^e) \end{aligned} \quad (21)$$

where e denotes each triangle of the cell surface formed by three vertices $\{\mathbf{y}_1^e, \mathbf{y}_2^e, \mathbf{y}_3^e\}$, and \mathbf{y}_c^e is an arbitrary point, which we choose to be the geometrical centre $\mathbf{y}_c^e = \sum_{i=1}^{N_c} \mathbf{y}_i^e / N_c$ with N_c the number of vertices in cell c . Figure 5 illustrates one of such triangles and tetrahedra.

The discretised energy functional mimics the definitions in (3), but with the previous measures of area and volume. In addition, and in order to ease the numerical convergence, the functional is minimised in consecutive pseudo-time steps $\Delta t = t_n - t_{n-1}$, which is tantamount to regularise the minimisation process. In summary, the following discrete energy functional is employed:

$$W^h(\mathbf{y}) = \left(\frac{V^h(\mathbf{y}) - V_0}{V_0} \right)^2 + \frac{\lambda_c}{n_A} \left(\frac{A_c^h(\mathbf{y})}{A_0} \right)^{n_A} + \frac{\lambda_e}{n_A} \left(\frac{A_e^h(\mathbf{y})}{A_0} \right)^{n_A} + \frac{\eta}{2} \|\Delta \mathbf{y}\|^2 \quad (22)$$

with $\Delta \mathbf{y} = \mathbf{y} - \mathbf{y}_{n-1}$ and η a regularisation parameter. For simplicity we denote by \mathbf{y} all the vertex positions $\mathbf{y}_1, \dots, \mathbf{y}_{N_{vert}}$ at current time t_n . In the results presented next, we let the geometry to evolve until

$\|\Delta y\| < 1e - 6\|\mathbf{y}\|$. At each time step t_n , the functional $W^h(\mathbf{y})$ is minimised with respect to the new positions \mathbf{y}_n , which is equivalent to solving the following system of non-linear equations:

$$\frac{\partial W^h(\mathbf{y})}{\partial \mathbf{y}_i} = \mathbf{0}, i = 1, \dots, N_{vert} \quad (23)$$

These equations are solved in an implicity manner, resorting to Newton-Raphson process. This requires the computation of the Jacobain. In Section (A) we detail the system of equations and the solution process.

The initial vertex positions \mathbf{y}_0 and triangularisation is constructed by defining a cloud of points, so called *nodes* \mathbf{x}_i , around the two estimated positions of the cell-centres. From these nodes, a Delaunay triangulation (tetrahedra in 3D) is built (shown as thin red lines in Figure 5a), and the vertices are placed at each barycentre of each tetrahedra. An additional vertex at each segment joining the cell centre \mathbf{y}_c and the connected nodes \mathbf{x}_i is added in order to have the external and common surfaces fully triangularised. The nodal network $\mathbf{x}_1, \dots, \mathbf{x}_{N_x}$ also allows to track cell-cell connectivity in case of topological transitions are allowed. The study of this transitions is under investigation and out of scope of the present paper.

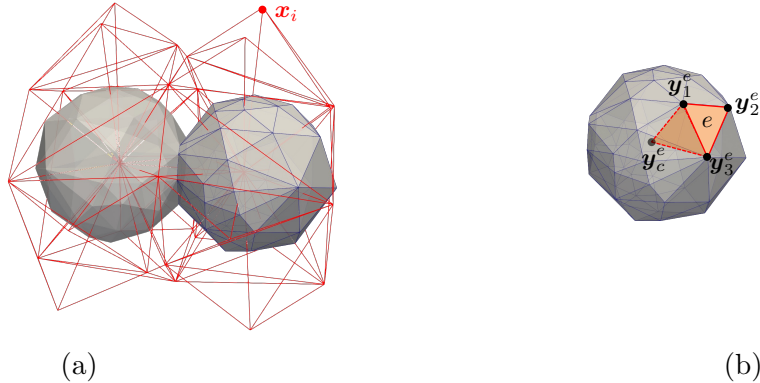


Figure 5: The geometry of 3D vertex model for two cells presented by a vertex network (dark lines) and nodal network (red thinner), shown in (a). Areas and volume are computed from the discretised triangularised surface of each cell, as depicted in (b).

This model is an extension of the previous work presented in [27], where the geometry was though limited to a monolayer, with two parallel apical and basal surfaces. Here, no restrictions on the geometry

are imposed, other than the size of the discretisation, which is regulated by the density of the nodal cloud. Models with finer density can be found for instance in [13, 29], which may be considered as an extension of the coarser vertex models.

3.2 Shape factor on discretised model

We have run the 3D vertex model using the linear and quadratic functionals. We have used a discretisation that is sufficient to estimate the shape factor h/r by fitting two spheres on the resulting set of vertices \mathbf{y}_i . The fitting was achieved by solving the following least squares problem:

$$\min_{h,r} \sum_i \|\mathbf{y}_i - P_{r,h}(\mathbf{y}_i)\|^2$$

where $P_{r,h}(\mathbf{y}_i)$ is the projection of vertex \mathbf{y}_i on the surface of two spheres of radius r and half overlapping equal to h . The axis that joints the two centres of the spheres and the mid plane is deduced from the whole set of vertices \mathbf{y}_i . Alternatively, we note that from the expressions in (9), the ratio of A_c and A_e is given by,

$$\frac{A_c}{A_e} = \frac{h}{2r}$$

Therefore, the shape factor h/r can be also estimated from the value of $2A_c/A_e$. Figure 6 shows the latter estimate, which coincides with a relative error smaller than 5% with respect to the first estimate. This figure also shows the theoretical results obtained in the previous section. As it can be observed, the shape factors of the vertex model confirm the theoretical results.

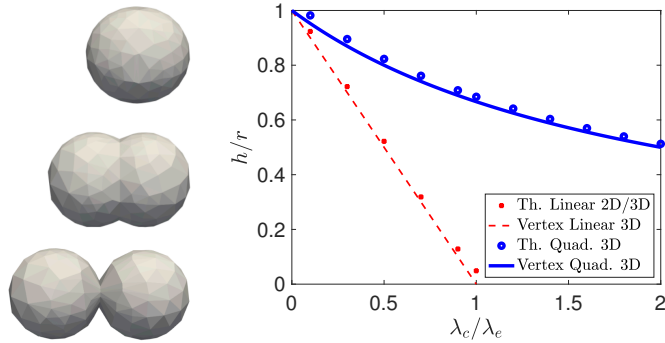


Figure 6: Comparison of theoretical results and those obtained from vertex 3D model.

4 Conclusions and discussion

The present paper has focused in two main contributions: i) derivation of analytical functional minimisers: radius in single cells, and shape factors in two-cells systems, and ii) development and validation of numerical model for analysing cell systems, regarded as those driven by volume constraints and contact area minimisations. Motivated by the different energy functionals employed in the literature, we have deduced the influence of linear and quadratic surface area terms in the functional.

In single cell analysis, we have deduced the presence of limit values of the surface tension in linear and quadratic functionals for 2D, but only for the linear case in 3D. In this last case, there is a minimum radius beyond which the cell collapses. In the quadratic case instead, the resulting radius can be reduced by further increasing λ_e . The presence of these limits is important prior to implementing numerical models for simulating cell responses.

In linear functionals, the contact angle is a direct experimental measure of the surface tension. We have shown that this angle reduces to 0 when λ_c approaches λ_e , while in the quadratic case such angle only vanishes in the limit case $\lambda_c/\lambda_e \rightarrow \infty$.

An important consequence of our analysis is that in all cases, linear and quadratic in 2D and 3D, the shape factor h/r only depends on the ratio the cell-cell and cell-media adhesion parameters, λ_c/λ_e , but not on their actual values. Moreover, the dependence of h/r on λ_c/λ_e is the same in 2D and 3D for linear analysis, but different for quadratic functionals. This result poses some limitations on the use of reduced simplified two-dimensional models when elastic surface responses are implemented.

The ability of VMs to include cell rearrangements and intercalation events is one of their most important features. The evolution is a mixture of mechanical equilibrium and alterations in tissue connectivity as a result of predetermined cell rearrangement processes. We have omitted here the analysis of such rearrangements, so-called T1 and T2 transitions in 2D [22]D, and we have also ignored more realistic local variations of the model parameters. There have been significantly fewer investigations into three-dimensional cell aggregations, which provide a number of computational obstacles as well as topological and geometrical complexities, requiring constant redefinition of cell connections in three dimensions. We leave this analysis and their dependence on the functional for further work.

The validation of the vertex model is a necessary step before considering and numerically simulating those complex situations. We have shown that they are valid models to reproduce the theoretical predictions in simple cases. In fact, the measurement of the trend of

the shape factor for different contractilities and cell-cell adhesive conditions may be an indirect manner to infer viscoelastic properties of cells, or additionally, to conclude whether cell behave more elastically, with a quadratic elasticity function, or in a fluid manner, with a linear functional and shape independent surface tension. Some studies indicate that cells such as S180, better fit the response of an elastic thin shell [47, 13], and thus quadratic functionals are more appropriate, at least on the short time regime (seconds). As we have shown here, for this case, reduced two-dimensional models give qualitatively different results and are not suitable. The study of the shape analysis of three-dimensional monolayers has been investigated for instance in [48]. The modelling of general multicellular systems and inhomogeneities with the current model is under investigation.

Acknowledgments

AKK is financially supported by the Higher Education Commission (under the Ministry of Federal Education and Professional Training) of Pakistan, and CO and JJM are financially supported by the Spanish Ministry of Science and Innovation, under grants PID2020-116141GB-I00 and CEX2018-000797-S.

Author contributions

AKK and JJM developed the analytical results. JJM implemented and generated the numerical results with the vertex model. JJM, KKA and CO studied the comparison of analytical and numerical results. All authors revised the manuscript.

Financial disclosure

None reported.

Conflict of interest

The authors declare no potential conflict of interests.

Ethical statement

Not applicable.

Supporting information

The following supporting information is available as part of the online article:

Video S1. Vertex model animation of the two-cells configuration for $\lambda/c/\lambda_e = 0$ and linear functional.

Video S2. Vertex model animation of the two-cells configuration for $\lambda/c/\lambda_e = 1$ and linear functional.

A . System of equations of the vertex model

The system of equations in (23) may be expressed as,

$$\begin{aligned} \left(\frac{V^h(\mathbf{y}) - V_0}{V_0} \right) \frac{\partial V^h}{\partial \mathbf{y}_i} + \frac{\lambda_c}{A_0^{n_A}} (A_c^h)^{n_A-1} \frac{\partial A_c^h}{\partial \mathbf{y}_i} \\ + \frac{\lambda_e}{A_0^{n_A}} (A_e^h)^{n_A-1} \frac{\partial A_e^h}{\partial \mathbf{y}_i} + \eta \Delta \mathbf{y}_i = \mathbf{0}, \\ i = 1, \dots, N_{vert} \end{aligned} \quad (24)$$

The derivatives of A^h and V^h with respect to the vertex positions \mathbf{y}_1 , \mathbf{y}_2 and \mathbf{y}_3 may be deduced from the expression in (21) as,

$$\begin{aligned} \frac{\partial A^h}{\partial \mathbf{y}_i} &= - \sum_{i \in C} \frac{1}{\|\mathbf{Y}_1 \mathbf{y}_2 + \mathbf{Y}_2 \mathbf{y}_3 + \mathbf{Y}_3 \mathbf{y}_1\|} (\mathbf{Y}_k^2 + \mathbf{Y}_l^2) \mathbf{y}_i \\ \frac{\partial V^h}{\partial \mathbf{y}_i} &= \mathbf{Y}_k \mathbf{y}_l + \mathbf{Y}_c (\mathbf{y}_k - \mathbf{y}_l) \end{aligned} \quad (25)$$

where ikl is a positive permutation of vertices 123, and \mathbf{Y} is the skew symmetric matrix form of a vector \mathbf{y} such that for any vector $\mathbf{a} \in \mathbb{R}^3$ we have that $\mathbf{y} \times \mathbf{a} = \mathbf{Y} \mathbf{a}$, with

$$\mathbf{Y} = \begin{bmatrix} 0 & -y_z & y_y \\ y_z & 0 & -y_x \\ -y_y & y_x & 0 \end{bmatrix}$$

The equation in (24) can be expressed as $\mathbf{g}(\mathbf{y}) = \mathbf{0}$, which is solved through a Newton-Raphson iterative process, which at each iteration k solves the following system of linear equations:

$$\delta \mathbf{y} = -\mathbf{K} \mathbf{g}(\mathbf{y}^k)$$

with $K = \frac{\partial \mathbf{g}}{\partial \mathbf{y}} \Big|_{\mathbf{y}=\mathbf{y}^k}$ the Jacobian matrix. The vertex coordinates are iteratively updated as $\mathbf{y}^{k+1} = \mathbf{y}^k + \delta \mathbf{y}$. Matrix \mathbf{K} can be derived from the expressions in (25). Convergence was accepted whenever $\max(\|\mathbf{g}(\mathbf{y}^k)\|, \|\delta \mathbf{y}\|) < 1e-10$. We have used the initial values $r_0 = 1$ and $\eta = 1.0$. The latter parameter has been incrementally decreased until $\eta = 1e-3$. At this point, the difference between time-steps satisfied $\|\Delta \mathbf{y}\| < 1e-3$.

References

- [1] Heisenberg CP, Bellaïche Y. Forces in Tissue Morphogenesis and Patterning. *Cell* 2013; 153(5): 948-962.
- [2] Lecuit T, Lenne P, Munro E. Force generation, transmission, and integration during cell and tissue morphogenesis. *Annu. Rev. Cell Dev. Biol.* 2011; 27: 157–184.
- [3] Dolega M, Delarue M, F.Ingremau , Prost J, Delon A, Cappello G. Cell-like pressure sensors reveal increase of mechanical stress towards the core of multicellular spheroids under compression. *Nat. Commun.* 2017; 8: 14056.
- [4] Gómez-González M, Latorre E, Arroyo M, Trepats X. Measuring mechanical stress in living tissue. *Nat. Rev. Phys.* 2020; 2: 300-317.
- [5] Serwane F, Mongera A, Rowghanian P, et al. *In vivo* quantification of spatially varying mechanical properties in developing tissues. *Num. Math.* 2017; 14: 181–186.
- [6] Thenard T, Catapano A, Mesnard M, Allena R. A Cellular Potts energy-based approach to analyse the influence of the surface topography on single cell motility. *J. Theor. Biol.* 2021; 509: 110487.
- [7] Nyga A, Muñoz J, Dercksen S, et al. Oncogenic RAS instructs morphological transformation of human epithelia via differential tissue mechanics. *Sc. Adv.* 2021; 7(42): eabg6467.
- [8] Oltean A, Taber L. A Chemomechanical Model for Regulation of Contractility in the Embryonic Brain Tube. *J. Elasticity* 2021; 145: 77–98.
- [9] Roldán L, Muñoz J, Sáez P. Computational modeling of epithelial wound healing: Short and long term chemo-mechanical mechanisms. *Comp. Meth. Appl. Mech. Engng.* 2019; 350: 25–56.
- [10] Alt S, Ganguly P, Salbreux G. Vertex models: from cell mechanics to tissue morphogenesis. *Philos. Trans. R. Soc. London B* 2017; 372: 20150520. <http://dx.doi.org/10.1098/rstb.2015.0520>.

- [11] Escribano J, Sánchez MT, García-Aznar JM. A discrete approach for modeling cell-matrix adhesions. *Comp. Part. Mech.* 2014; 1: 117-130.
- [12] Mirams G, Arthurs C, Bernabeu M, et al. Chaste: An Open Source C++ Library for Computational Physiology and Biology. *PLOS Comp. Biol.* 2013; 9(3): e1002970.
- [13] Smeets B, Pešek MCJ, Ramon H. The Effect of Cortical Elasticity and Active Tension on Cell Adhesion Mechanics. *Bioph. J.* 2019; 116(5): 930–937.
- [14] Honda H, Tanemura M, Nagai T. Geometrical Models for Cells in Tissues. *Int. Rev. Cytol.* 1983; 1983(81): 191-248.
- [15] Weaire D, Rivier N. Soap, cells and statistics—random patterns in two dimensions. *Cont. Phys.* 1984; 25: 59–99.
- [16] Honda H, Nagai T. Cell models lead to understanding of multicellular morphogenesis consisting of successive self-construction of cells. *J. Biol. Chem.* 2015; 157: 129–136.
- [17] Huang J, Cochran J, Fielding S, Marchetti M, Bi D. Shear-driven solidification and nonlinear elasticity in epithelial tissues. *Phys. Rev. Letters* 2022; 128(17): 178001.
- [18] Nagai T, Honda H. A dynamic cell model for the formation of epithelial tissues. *Phil. Mag. Part B* 2001; 81: 699-719.
- [19] Farhadifar R, Röper JC, Aigouy B, Eaton S, Jülicher F. The influence of cell mechanics, cell-cell interactions, and proliferation on epithelial packing. *Current Biol.* 2007; 17: 2095–2104.
- [20] Perez-Verdugo F, Banerjee S. Tension remodeling controls topological transitions and fluidity in epithelial tissues. *Arxiv* 2022: 1–16. <https://doi.org/10.48550/arXiv.2211.05591>.
- [21] Salbreux G, Barthel LK, Raymond PA, Lubensky DK. Coupling Mechanical Deformations and Planar Cell Polarity to Create Regular Patterns in the Zebrafish Retina. *PLOS Comp. Biol.* 2012; 33: 469-502.
- [22] Bi D, Lopez J, Schwarz J, Manning M. A density-independent rigidity transition in biological tissues. *Nat. Phys.* 2015; 11: 1074-1079.
- [23] Latorre E, Kale S, Casares L, et al. Active superelasticity in three-dimensional epithelia of controlled shape. *Nature* 2018; 563(7730): 203–208.
- [24] Tang W, Das A, Pegoraro A, et al. Collective curvature sensing and fluidity in three-dimensional multicellular systems. *Nat. Phys.* 2022; 18: 1371–1378.

- [25] Monier B, Gettings M, Gay G, et al. Apico-basal forces exerted by apoptotic cells drive epithelium folding. *Nature* 2015; 7538: 245–8.
- [26] Honda H, Motosugi N, Nagai T, Tanemura M, Hiiragi T. Computer simulation of emerging asymmetry in the mouse blastocyst. *Development* 2008; 135(8): 1407-1414.
- [27] Ioannou F, Dawi M, Tetley R, Mao Y, Muñoz J. Development of a new 3D hybrid model for epithelia morphogenesis. *Front. Bioeng. Biotechnol.* 2020; 10: 1–11.
- [28] Bielmeier C, Alt S, Weichselberger V, et al. Interface Contractility between Differently Fated Cells Drives Cell Elimination and Cyst Formation. *Current Biol.* 2016; 25: 563–574.
- [29] Cuvelier M, Thiels W, Jelier R, Smeets B. Stability of asymmetric cell division under confinement: A deformable cell model of cytokinesis applied to *C. elegans* development. *Bioarxiv* 2023: 1–18.
- [30] Fang Y, Lai KWC. Modeling the mechanics of cells in the cell-spreading process driven by traction forces. *Phys. Rev. E* 2016; 93: 042404.
- [31] Trichas G, Smith A, White N, et al. Multi-cellular rosettes in the mouse visceral endoderm facilitate the ordered migration of anterior visceral endoderm cells. *Phys. Biol.* 2012; 10: e1001256.
- [32] Duclut C, Paijmans J, Inamdar MM, Modes CD, Jülicher F. Non-linear rheology of cellular networks. *Cells & Dev.* 2021: 203746.
- [33] Barton D, Henkes S, Weijer C, Sknepnek R. Active Vertex Model for cell-resolution description of epithelial tissue mechanics. *PLOS Comp. Biol.* 2017; 13(6): 1-34.
- [34] Osterfield M, Du XX, Schüpbach T, Wieschaus E, Shvartsman SY. Three-Dimensional Epithelial Morphogenesis in the Developing *Drosophila* Egg. *Dev. Cell* 2013; 24(1): 400-410.
- [35] Fletcher A, Osborne J, Maini P, Gavaghan D. Implementing vertex dynamics models of cell populations in biology within a consistent computational framework. *Prog. Biophys.Mol.Biol.* 2013; 113(2): 299 - 326.
- [36] Bi D, Yang X, Marchetti MC, Manning ML. Motility-Driven Glass and Jamming Transitions in Biological Tissues. *Phys. Rev. X* 2016; 6: 021011.
- [37] Spencer MA, Jabeen Z, Lubensky DK. Vertex stability and topological transitions in vertex models of foams and epithelia. *Eur. Phys. J. E* 2017; 40: 1–17.
- [38] Cavanaugh K, Staddon M, Munro E, Banerjee S, Gardel M. RhoA mediates epithelial cell shape changes via mechanosensitive endocytosis. *Dev. Cell* 2020; 52(2): 152-166.

- [39] Mosaffa P, Asadipour N, Millán D, Rodríguez-Ferran A, Muñoz J. Cell-centred model for the simulation of curved cellular monolayers. *Comp. Part. Mech.* 2015; 2(4): 359–370.
- [40] Mosaffa P, Rodríguez-Ferran A, Muñoz J. Hybrid cell-centred/vertex model for multicellular systems with equilibrium-preserving remodelling. *Int. J. Num. Meth. Biomed. Engng.* 2018; 34(3): 1–24.
- [41] Mosaffa P, Tetley R, Rodríguez-Ferran A, Mao Y, Muñoz J. Junctional and cytoplasmic contributions in wound healing. *J. R. Soc. Interface* 2020; 17: 20200264.
- [42] Honda H, Tanemura M, Nagai T. A three-dimensional vertex dynamics cell model of space-filling polyhedra simulating cell behavior in a cell aggregate. *J. Theor. Biol.* 2004; 226: 439–453.
- [43] Okuda S, Inoue Y, Eiraku M, Sasai Y, Adachi T. Modeling cell proliferation for simulating three-dimensional tissue morphogenesis based on a reversible network reconnection framework. *Biomech. Model. Mechanobiol.* 2013; 12: 987–996.
- [44] Misra M, Audoly B, Kevrekidis I, Shvartsman S. Shape Transformations of Epithelial Shells. *Bioph. J.* 2016; 110(7): 1670–1678.
- [45] Brochard-Wyart F, de Gennes PG. Unbinding of adhesive vesicles. *Comptes Rendus Physique* 2003; 4(2): 281–287.
- [46] Gennes dF. *Capillarity and Wetting Phenomena: Drops, Bubbles, Pearls, Waves.* Springer . 2004.
- [47] Chu Y, Dufour S, Thiery J, Perez E, Pincet F. Johnson-Kendall-Roberts theory applied to living cells. *Phys. Rev. Letters* 2005; 94: 028102.
- [48] Hannezo E, Prost J, Joanny J. Theory of epithelial sheet morphology in three dimension. *Proc. Natl. Acad. Sci. USA* 2014; 111(1): 27–32.